UCLA
UCLA Previously Published Works

Title
An Ex Vivo Study of Outward Electrical Impedance Tomography (OEIT) for Intravascular Imaging

Permalink
https://escholarship.org/uc/item/6364g278

Journal
IEEE Transactions on Biomedical Engineering, 69(2)

ISSN
0018-9294

Authors

Luo, Yuan
Huang, Dong
Huang, Zi-Yu
et al.

Publication Date
2022-02-01

DOI
10.1109/tbme.2021.3104300

Peer reviewed

An *ex vivo* Study of Outward Electrical Impedance Tomography (OEIT) for Intravascular Imaging

Yuan Luo[†,*],

State Key Laboratory of Transducer Technology, Shanghai Institute of Microsystem and Information Technology, Chinese Academy of Sciences, Shanghai, 200050, China

Center of Materials Science and Optoelectronics Engineering, University of Chinese Academy of Sciences, Beijing, 100049, China

Department of Medical Engineering, California Institute of Technology, Pasadena, CA 91125, USA

Dong Huang[†],

College of Engineering; Institute of Microelectronics, Peking University, Beijing, China

Zi-Yu Huang[†],

Department of Medical Engineering, California Institute of Technology, Pasadena, CA 91125, USA

Tzung K. Hsiai,

Department of Bioengineering, Division of Cardiology, Department of Medicine, David Geffen School of Medicine, University of California, Los Angeles, Los Angeles, CA 90095, USA

Yu-Chong Tai [Fellow, IEEE]

Department of Medical Engineering, California Institute of Technology, Pasadena, CA 91125, USA

Abstract

Objective: Atherosclerosis is a chronic immuno-inflammatory condition emerging in arteries and considered the cause of a myriad of cardiovascular diseases. Atherosclerotic lesion characterization through invasive imaging modalities is essential in disease evaluation and determining intervention strategy. Recently, electrical properties of the lesions have been utilized in assessing its vulnerability mainly owing to its capability to differentiate lipid content existing in the lesion, albeit with limited detection resolution. Electrical impedance tomography is the natural extension of conventional spectrometric measurement by incorporating larger number of interrogating electrodes and advanced algorithm to achieve imaging of target objects and thus provides significantly richer information. It is within this context that we develop Outward Electrical Impedance Tomography (OEIT), aimed at intravascular imaging for atherosclerotic lesion characterization.

---

[*]correspondence: yuanluo@mail.sim.ac.cn.

[†]Y. Luo, D. Huang and Z.-Y. Huang contribute to this work equally.

Methods: We utilized flexible electronics to establish the 32-electrode OEIT device with outward facing configuration suitable for imaging of vessels. We conducted comprehensive studies through simulation model and *ex vivo* setup to demonstrate the functionality of OEIT.

Results: Quantitative characterization for OEIT regarding its proximity sensing and conductivity differentiation was achieved using well-controlled experimental conditions. Imaging capability for OEIT was further verified with phantom setup using porcine aorta to emulate *in vivo* environment.

Conclusion: We have successfully demonstrated a novel tool for intravascular imaging, OEIT, with unique advantages for atherosclerosis detection.

Significance: This study demonstrates for the first time a novel electrical tomography-based platform for intravascular imaging, and we believe it paves the way for further adaptation of OEIT for intravascular detection in more translational settings and offers great potential as an alternative imaging tool for medical diagnosis.

I. Introduction

Atherosclerosis is a chronic disease manifested as localized built-up of substance (also known as plaques) on the arterial wall due to complicated interplay of lipoprotein retention, inflammatory reaction and cellular metabolic dynamics [1]. The growth of these atherosclerotic plaques results in the narrowing of arterial lumen, and more severely, when the plaques advance to later stages they are highly prone to rupture [2]. Such rupturing leads to precipitating thrombi at the initial sites or embolism at downstream sites, possibly completely obstructing the essential blood flow. The most critical conditions caused thereof include the occlusion of coronary arteries (resulting in myocardial infarction) and carotid arteries (ischemic stroke) [3]. Atherosclerosis is widely considered as the leading cause of mortality and morbidity in the world [4]. The assessment of the vulnerability of these atherosclerotic lesions has been a critical topic for cardiovascular research, which leads to the development of a plethora of invasive/non-invasive imaging modalities for atherosclerosis diagnosis.

Frequently adopted non-invasive imaging modalities, including Computed Tomography (CT)/Coronary CT Angiography (CCTA), Magnetic Resonance Imaging (MRI), Ultrasound, positron emission tomography (PET), and multi-modal imaging strategies combining individual techniques, can provide important insight in lesion evaluation, especially in the case of low to medium risk patients [5–8]. However, even with the recent technological advancement for non-invasive modalities, invasive imaging tools are still considered to offer the highest resolution images with in-depth analysis on artery wall composition and plaque morphology, especially for high risk patients with severe symptoms [9]

Among existing invasive techniques, catheter angiography and flow fractional reserve (FFR) have become the routine procedures once the patient show severe symptoms (e.g.

stable angina). However, these methods can only measure stenosis and merely provides a lumenogram of the coronary circulation without any specific knowledge on the actual plaque composition [6]. Intravascular ultrasound (IVUS) [10] and optical coherence tomography (OCT) [11] have been the other clinically available options for intravascular imaging, both with varying degree of success in atherosclerotic plaque characterization. However, IVUS yields unsatisfactory results in tissue characterization due to insufficient resolution and is limited by a certain degree of subjectivity from operator's interpretation [12]. On the other hand, despite the excellent spatial resolution it provides, OCT lacks the penetration depth for full vessel wall coverage and often requires frequent saline flushing to fence off red blood cells interference during imaging processing [7]. Near infrared spectroscopy (NIRS) is another emerging modality for specific lipid content characterization, yet still at its early stage and facing challenge in obtaining quantitative information about size and location of the lipid core [13].

Recent efforts in intravascular detection see a new direction in exploiting the electrical characteristics of atherosclerotic lesions as an evaluation criterion [14–17]. The fundamental impetus is to target one of the well-recognized feature of vulnerable atherosclerotic plaques, the lipid-rich pool, as lipid exhibits a drastically different electrical conductivity than the cell-laden normal vessel tissues, almost an order of magnitude in difference on average [18]. This desirable feature could lead to unique capability in identifying the different degrees of plaque vulnerability [19]. Moreover, electrical current naturally posts deeper penetration and is suitable for imaging vessel walls that are typically of thickness around 2~3 mm. These advantages spurred the interest in the pursuit of adopting electrochemical impedance spectroscopy (EIS) as a new intravascular detection tool. To the best of our knowledge, existing impedance-based methods rely only on measuring the impedance spectrum from target tissues with limited number of electrodes. The most glaring issue is the rather poor resolution in interrogating the vessel. After all, none of the EIS-based intravascular studies can provide "true" imaging of the vessel [17].

Fortunately, converting impedance-based measurement to imaging of target objects has already been achieved through several tomography-based techniques. Among these, electrical impedance tomography (EIT), has gained tremendous attention and witnessed a wide range of clinical applications in the past decades [20, 21]. It uses electrode array attached on the outer surface of an object and reconstructs the conductivity distribution of the object by sending electrical current and measuring response in a predefined pattern. The configuration in which electrode array encircling the targets from outside also partially results in EIT being typically applied in imaging human thoracic area [22], and also adaptation in brain imaging in recent years [23, 24]. In the context of intravascular imaging, a reverse configuration as opposed to typical EIT implementation is required for such tubular target, where electrode array needs to be situated inside the vessel lumen and images outward. EIT design applicable for such tubular organ also has great implication in other medical imaging scenarios, yet demonstration of device along this vein is limited except for its application in endoscopic navigation of prostate diagnosis [25–27].

The potential of utilizing EIT in intravascular imaging is apparently tremendous owing to the distinct electrical signature of atherosclerotic lesion, and yet has remained essentially

untapped, except for simulation studies in predicting its feasibility [28, 29]. We herein develop outward electrical impedance tomography (OEIT), in an attempt to exploit such great potential. As depicted in Fig. 1, we designed and established a catheter-based device with 32 individual electrodes embedded in flexible substrate. We conducted comprehensive characterization of the imaging performance through both simulation studies and experimental settings with well-defined boundaries. We further demonstrated intravascular imaging in proximity detection and fatty tissue identification in an *ex vivo* phantom setup emulating clinical conditions. With these studies we successfully established the functionalities of the OEIT system and laid the foundation for further *in vivo* verification and adaptation in the near future.

II.   Method

A.   EIT Theory

The mathematical foundation of EIT has been detailed elsewhere [20]. In brief, EIT is set out to solve the inverse problem of the Laplace equation. As an analytical solution is extremely difficult to obtain, most EIT algorithm relies on numerical method to achieve a desired solution. Among those, the Gauss-Newton (GN) type solver gain tremendous success and its general concept starts with defining an error variable:

$$\varepsilon = V_m - L^*(\sigma) \tag{1}$$

where σ denotes the target conductivity distribution, V_m is the measured voltage values obtained from experiment, and $L^*(\sigma)$ represents a voltage function on σ implicitly defined from the Laplace equation $\nabla \cdot (-\sigma \nabla V) = 0$. To find the optimal σ, the GN solver seeks to minimize the L-2 norm of (1) with the first order Taylor expansion approximation of $L^*(\sigma)$:

$$E = \left\| \varepsilon \right\|^2 = \left\| V_m - L^*(\sigma) \right\|^2 \cong \\ \left\| (V_m - L^*(\sigma_0)) - J(\sigma - \sigma_0) \right\|^2 \tag{2}$$

where σ_0 is a reference conductivity distribution and J denotes the Jacobian matrix corresponding to $L^*(\sigma)$. The notorious ill-posedness of the inverse problem of EIT renders a stable solution for minimizing (2) rather impossible. The common technique to tackle this issue is by adding regularization terms and (2) becomes:

$$E^r = \left\| \varepsilon \right\|^2 + \lambda \left\| \Gamma \sigma \right\|^2 \tag{3}$$

where λ is called the regularization parameter, which can be chosen properly based on the actual inverse problem to stabilize the final solution. Γ provides further degree of freedom for manipulating the solution [30]. The minimization is achieved through solving $E^r / \sigma = 0$ and we can obtain:

$$\sigma_1 = \sigma_0 + \left(J^T J + \lambda \Gamma^T \Gamma \right)^{-1} J^T (V_m - L^*(\sigma_0)) \tag{4}$$

To calculate the absolute conductivity distribution, an iterative scheme needs to be implemented. The initial conductivity value σ_0 is obtained by an educated guess (could be an uniform distribution), which was then used to calculate the Jacobian matrix J, obtain L^*, and eventually generate a first conductivity distribution σ_1. This scheme is continued until the difference between σ_n and σ_{n+1} is smaller than the predefined tolerance.

B. EIDORS Implementation

The imaging algorithm described above was implemented with the help of the online open source library, EIDORS [31]. The library allows designing the finite element models with precise geometries and proper meshing. The implementation of our OEIT requires distinct model geometry as compared to typical thoracic imaging. As shown in Fig. 2, a cylindrical structure was first created followed by removing a smaller inner cylinder, resulting in a "donut" shape domain of interest (DOI), with the electrodes placed in the inner wall surface. The inner cylinder represented the space occupied by the device and hence was assumed to be excluded from our DOI. There were two different scenarios regarding the specific geometric parameters adopted in the model (see case I & II detailed in Fig. 3). In case I, we set the inner cylinder diameter (d) to be that of the device (5 mm). We chose to ignore all the possible influence originating from outside the vessel by setting the outer cylindrical boundary (D) to be diameter of the vessel (13.5 mm) because the focus in this scenario is to detect the existence of a lipid rich pool surrounded by the conductive solution environment inside the vessel. Hence the DOI in this case is the red region in Fig. 3a. The relative position between the device and the vessel wall is generally unchanged and maintained a concentric configuration (see experimental details in sections III-C & III-E). On the other hand, case II is intended for the proximity detection experiment (section III-B & III-D): while the inner cylinder in the model is still kept the same size as the actual device, the outside cylindrical boundary needs to fulfill one requirement: its radius R needs to be larger than $D - d/2$ in order to accommodate the most eccentric condition caused by the relative movement between device and vessel (see the dotted circle in Fig. 3b for illustrating the extreme condition). In the actual model we directly set $R = D$ and therefore resulting in the DOI in blue region in Fig. 3b.

For our simulation study, case I was adopted and an ellipsoid structure was also created within the DOI with proper conductivity to mimic fatty tissue (Fig. 2b). We first carried out the forward calculation in solving the time harmonic form of Laplace equation [30]. The solutions gave us a mock voltage measurement which could be used as input to generate a new conductivity mapping by numerically solving (4). For imaging the experimental data, the measured voltages from different settings were fed to their corresponding models, which subsequently calculated the conductivity distribution via the regularized Gauss-Newton solver. We finally adopted a previously reported method [30] to identify the region of interest from the resulting EIT images for further analysis.

C. Device Design and Fabrication

As shown in Fig. 1, the fabrication of OEIT device started from flexible electrodes (20 cm in length) with polyimide-copper-polyimide sandwich structure ordered from outside supplier (FPCexpress, Ontario, Canada). Electrode pattern was designed as follows: there were total

32 individual electrodes placed on the polyimide sheet with each electrode being 200 μm wide and also separated with 200 μm interspace. The exposed length for each electrode was set as 1 mm. A 3D printed cylindrical rod with 5-mm diameter (Craftbot Plus, CraftUnique, Hungary) serve as the substrate which the flexible electrode was rolled onto and both edges of the polyimide sheet were glued together with silicon adhesive (Henkel, CT). Contact pad arrays (5 mm×5 mm) were located on the distal end of the flexible electrode (Fig. 1c) where copper wires were soldered and secured with epoxy. The wires were further connected to the 32 individual channels from the data acquisition equipment.

D. Samples and Reagents

Sodium Chloride solution was dissolved in deionized (DI) water to various concentrations of wt % (0.0563%, 0.1125%, 0.225%, 0.45%, 0.9% (normal saline concentration)) to reach different conductivity values: 0.11-, 0.25-, 0.45-, 0.85- and 1.60-S/m, respectively. The actual conductivity of the solution was confirmed using a benchtop conductivity meter (Mettler-Toledo, OH). A cylindrical container (Polylactic acid, PLA) was 3d printed (Craftbot Plus, CraftUnique, Hungary) to form the well-defined boundaries for device characterization experiment. Porcine aortas and fresh whole blood were purchased from a local animal tissue provider with same day delivery (Sierra Medical, CA). The aortas were cut in short segments (~10 cm long) to meet the experimental needs and their diameter was measured at around 13.5 mm. Large volume of fat was purchased from a local supermarket and cut into small pieces to fit in the experimental setting.

E. Hardware

The experiment was conducted on a planar XY-stage with manual control at 0.01 mm resolution. The OEIT device was secured on a separate support stand with clamping fastener and held steady throughout the experiment. The rest of the experimental phantom was affixed on the XY-stage and subject to controlled horizontal movement. All of the electrical measurements for OEIT imaging were conducted using SenTec EIT Pioneer set (SenTec AG, Switzerland). The excitation was kept at 3 mA and 250 kHz. Both the current injection and voltage measuring pattern was following the previously reported protocol of "skip 4" [30], namely, there were four idle electrodes between the selected pair for either current injection or voltage acquisition.

III. Results

A. Simulation

We firstly conducted a series of simulation study to verify the OEIT imaging model established using EIDORS. We created a heterogeneous conductivity distribution within the DOI to mimic the existence of fatty tissue (elliptical, Fig. 2b). The conductivity of the white region was set at 0.85 S/m, the same as that of the blood. The conductivity within the ellipse was then set in a range varying from 0.02–0.10 S/m in reference to the typical conductivity value for fatty tissue to be ~0.04 S/m[18]. The imaging results calculated from our model captured the elliptical shape (representative image in Fig. 2c, full set of images in supplementary materials Fig. S1). We further identified the regions of interest from the initial imaging results (supplementary materials Fig. S1) and estimated the average

conductivity values within them, which exhibited a linear correlation between the nominal and calculated conductivity values (Fig. 2d). These results demonstrated the efficacy for our imaging model ready for experimental verification.

B. Proximity Measurement

After the information obtained with simulation, we proceeded to experimentally demonstrate the imaging capability of the OEIT device. First, we conducted a proximity detection study in an experimental setup with well-defined conditions. As shown in Fig. 4a–b, a cylindrical container filled with 0.45% wt NaCl solution was fixed on the mobile track of the XY-stage. The OEIT device was clamped on a support stand and its distal end (with electrodes) reaching to the interior of the container. The container movement in the horizontal plane was controlled by the XY-stage with high accuracy (0.01mm). Such experimental condition mimicked the movement of intravascular device being deployed within the conductive aqueous environment inside the blood vessels. We sought to monitor the proximity of the OEIT device with respect to the sidewall of the container. The distance between the edge of the device and the sidewall of the container in the radial direction was used as the indicator (symbol "p" in Fig. 4b), both in the actual physical measurement, and in the resulted images. The relative position between the device and the container can be precisely controlled by moving the XY-stage. The distance p was varied from 0 to 3.75mm with 0.25mm step size. For every such position, current injection and voltage acquisition were conducted and used to generate the impedance tomography. Fig. 4c presents a sequence of four images with increasing distance p. We adopted the case II EIDORS model described above. The red region in the images represented high conductivity (around 0.8S/m), whereas the blue region denoting low conductivity reflected the container sidewall, as well as the air space outside the container. As seen, the transition appeared to be rather sharp between these two distinct regimes, which was the result of a drastically different conductivity value between the NaCl solution (0.85 S/m) and the insulating PLA material [32]. From every such conductivity mapping, we further measured the corresponding p value. The correlation between these two sets of "p" was plotted in Fig. 4d, which demonstrated a reasonable agreement except a small offset of ~ 1mm. We suspected this could be due to the fact that in the actual measurement, there can still be a narrow gap of solution between the electrodes and the sidewall even when the device was "touching" the sidewall, which then caused the reconstruction algorithm to "infer" existence of conductive medium. Such error could be further calibrated in the imaging algorithm.

C. Conductivity Characterization

Next, we investigated the characteristics of conductivity sensing by OEIT and its differentiating capability within the same experimental setup. As shown in Fig. 5a–b, a piece of fatty tissue was immersed inside the NaCl solution to create the non-homogeneous conductivity distribution as in the intravascular environment. In addition to the 0.45% wt NaCl (0.85 S/m) solution, we also tried to vary the solution conductivity values to assess its influence on the imaging quality. We hypothesized the impact of solution conductivity value on the differentiating capability of the OEIT inside a blood vessel environment can be qualitatively illustrated with the conceptual plot in Fig. 6. Here, we focus on the difference in impedimetric sensing data induced by adding the fatty tissue to an otherwise

homogeneous conductivity distribution within the solution: $Z = Z_n - Z_h$, Z_n and Z_h being the measured results for non-homogeneous (with fat) and homogeneous condition, respectively. In essence, there are two special cases that confine the limits for the outcome. First, when the conductivity of the blood is extremely high (imagine it is as conductive as metal), then due to current shorting caused, there would not be any noticeable change in any electrical measurement. The second case is when the blood has the exact same conductivity as the fatty tissue (a critical value in this conceptual curve), apparently there would also not be any differentiation no matter how the fatty tissue change its shape. And the optimal condition must lies between these two limiting cases.

Fig. 5c presents the imaging result generated from two solution conductivities (i.e. 0.11- and 0.85-S/m). We adopted the case I EIDORS model described above. We subsequently identified the regions of interest representing the fatty tissue as "seen" by our device and estimated both the average conductivity and the overall area from those regions for all five conditions (i.e., 0.11-, 0.25-, 0.45-, 0.85- and 1.60-S/m; Fig. 5d, full set of imaging results in supplementary materials Fig. S2). In general, our platform managed to identify the existence of the fatty tissue for all conditions. It is notable that by comparing data among all five conditions, the estimated area for the lowest solution conductivity (0.11 S/m) shows a significant drop (33%), whereas the fatty tissue conductivity from the highest solution conductivity case (1.6 S/m) also exhibits dramatic decrease (77%), from the other four conditions. Both noteworthy deviations can be an indication of the above-mentioned conductivity effect hypothesis, and the optimal scenario from a conductivity standpoint lies among the intermediate conductivity values.

Our findings suggested the potential benefit of tuning the conductivity of liquid environment during plaque detection for better differentiation. In actual clinical settings, tools for the *in vivo* liquid exchange during the catheterization procedure are readily available. For instance, it is common practice in OCT imaging to conduct saline flushing to expel the blood around the vicinity of the device in order to improve image quality [5, 33]. Our group has also demonstrated a double-balloon catheter design in which the small section of the artery flow can be isolated to achieve local drug delivery and potentially exchanging blood for other solution of distinct conductivity [34]. The integration of such double-balloon structure with flexible electrode for device prototype is within the design and fabrication capacity in our laboratory settings.

D. Proximity Detection in Aorta

After the characterization of our OEIT device in the previous setup with well-defined tubular boundaries, we advanced to adapt a porcine aorta for establishing a phantom setup to mimic *in vivo* condition. As shown in Fig. 7a–b, the aorta segment was placed concentrically on the bottom of a plastic container and secured with non-conductive epoxy. The container was then affixed on the XY-stage. Subsequently, we filled NaCl solution of different conductivity inside and outside the aorta segment. The inner lumen space was filled with 0.45% wt NaCl to mimic blood conductivity, whereas the rest of the space within the container was filled with 0.225% wt NaCl to match the general conductivity value of connective tissue [18]. We believed these configurations presented close approximation for the intravascular

environment. We performed a similar experiment as section III-B by moving the XY-stage to realize different proximity condition between the device and the aorta sidewall.

Fig. 7c shows a set of images from a sequence of varied relative positions between the pig aorta and the device. The DOI for the EIDORS model adopted here was the second scenario described above (Case II in Fig. 3). The middle panel in Fig. 7c presents the original reconstruction results for all five locations. As seen, the algorithm managed to capture the correct relative position of the device inside the aorta lumen. In the bottom panel of Fig. 7c, we performed post-processing on the resulted images by setting the conductivity value to an intermediate range, which only captures the "black" regions (see detailed explanation in supplementary materials Fig. S3) and served to further identify the shape of the aorta from the images. Of note, the shape of the aorta started to diverge from the actual circular shape when part of it was moving further away from the electrodes. This result possibly indicated the limitation of OEIT to image far field objects (>5 mm), yet it did not seem to affect proximity detection or the lipid identification as detailed in the subsequent section.

The navigation of the catheter inside the vessels during its deployment operation is crucial for the safety of intravascular intervention. The failure to conduct such deployment in a proper way could even cause severe damage to the vessels due to the catheter accidentally piercing through the tissue. The current guiding method is to rely on short duration of X-ray imaging [35], whereas the proximity detection capability of our device offers an attractive alternative. In contrast to the extra dosage of X-ray exposure, the EIT imaging, as described earlier, functions by simply sending small amount of current and causes no hazardous effect during the procedure. Note that the characteristic shift of electrical response resulted from the change of distance between the electrodes and target tissue has been exploited for cardiac disease applications. Kim *et al.* demonstrated *in vivo* monitoring of device contact with cardiac tissue based on impedance measurement [35]. We believe OEIT as an imaging modality showing full cross-sectional view of the lumen, can potentially offer better navigation performance.

E. Lipid Identification in Aorta

The key functionality of an intravascular imaging modality is the capability of assessing atherosclerotic lesions within the vessel environment. We proceeded to place fatty tissue inside the aorta to further emulate the existence of plaques (Fig. 8a). We switched the position of the fat tissue and used the electrode as the position marker (Fig. 8b). The four selected positions corresponded to #1, #10, #18, and #25 electrodes. The fatty tissue was measured and subsequently imaged at each position. The DOI for the EIDORS model adopted here was the first scenario described above (Case I in Fig. 3). As shown in Fig. 8c, fatty tissue located at the four locations can be identified with fairly good accuracy. The averaged conductivity and estimated area of the regions of interest (identified from original imaging, full set shown in supplementary materials Fig. S4) was also calculated and plotted in Fig. 8d. The average conductivity value obtained from these four different positions was 0.101S/m, which corresponded to around 0.03 S/m based on our simulation results (Fig. 2d) and is within reasonable range with reported values [18].

To further test the applicability of OEIT for more relevant intravascular conditions, as well as experimentally study the detection resolution for OEIT, we proceeded to conduct a new set of experiment by replacing saline solution with real blood in the above-described setting, and using fat tissue of various sizes. As shown in Fig. 9a–b, we used a set of four different fat tissue with the cross-sectional dimension measured at 15×3 mm^2, 9×3 mm^2, 5×3 mm^2, 3×3 mm^2, respectively. Fig 9c reveals the imaging results for the 9×3 mm^2 piece situated on #1, #10, #18, and #25 similar to the previous experiment, whereas Fig. 9d shows all four fat tissues placed on #18 position. A full set of imaging results showing all sizes fat tissue on all locations is available in supplementary materials (Fig. S5).

Based on these imaging results, it is obvious that switching the saline solution to real blood did not impact the imaging capability of OEIT. Another concern about the clinical relevance for our testing condition is the pulsatile nature of blood flow. We have conducted live animal study in previous work whereby impedance sensor was attached on the intervening catheter and directly measured impedance response *in vivo* within the arteries while monitoring the normal heart rate of the animal [16, 17]. The results in these studies suggested the pulsatile condition does not produce any noticeable disturbance on impedance sginal as compared to subjecting the same device under steady saline solution.

Next, we further extract the region of interest from all the images obtained from the experiment (supplementary materials Fig. S5) and calculate their effective area stenosis (i.e. the percentage of total cross-sectional area of the aorta lumen occupied by the fat tissue). For the real sample, the area stenosis was calculated to be 31.4%, 18.9%, 10.5%, 6.3%, with their respective cross-sectional area listed above divided by lumen area $\pi \times (13.5\text{mm}/2)^2$ $=143.14\text{mm}^2$. These two sets of values were compared as shown in Fig. 9e. We first noted that, though OEIT device was able to image fat tissue of all sizes in all locations successfully, the results for the smallest size were at a lower clarity compared to other three cases with larger sizes (Fig. 9c, Fig. S5). Statistical comparison in Fig. 9e also shows that the deviation in area stenosis values between real sample and tomographic imaging extracted results is within 35%, except the case with fat tissue of smallest size, which has a 6 times difference in area stenosis. These results indicated we are approaching the resolution limit under the current device design and experimental set-up with 6.3% area stenosis. On the other hand, it is reasonable to believe that our OEIT has the resolution to identify features as small as 10% of the total luminal area.

To evaluate the translational relevance of these results, consider an atherosclerotic lesion with diameter stenosis 25%, which corresponds to roughly 49% area stenosis [36]. This is considered "mild atherosclerosis" according to SCCT (The Society of Cardiovascular Computed Tomography) grading scale for stenosis severity [37]. A study of 55 patients reveals an average FFR at ~0.86 while the average area stenosis is ~47% [38]. An FFR value of 0.86 is still significantly above the 0.8 threshold in plaque vulnerability assessment from standard procedure, which means an area stenosis even higher than 47% is required for an FFR positive test. Comparison between these statistics and our experimental results suggests that OEIT is sufficient to be applied in intravascular imaging of clinically significant plaques.

IV. Discussion

It has been generally accepted that the atherosclerotic plaques that are vulnerable to rupture presents the most severe threat to cause acute and catastrophic events [3]. Such high risk plaques manifest itself with the signature features of a thin fibrous cap and a lipid rich necrotic core, which is formed by macrophage-turned foam cell engulfing large amount of lipid from the blood flow and later go through necrosis and releasing them [2]. The growing of the necrotic core also contributes to the continuous thinning of the fibrous cap. The rupturing is believed to be in large part the result of the reduction in mechanical strength of the fibrous cap [2], yet it is the necrotic core with significant lipid content that presents valuable opportunity for using electrical property-based tools for detection. Under such circumstances, the amount of fibrous material, such as fibrin, is reduced significantly. On the other hand, lipid content, including cholesterol, becomes a strong indicator for determining the propensity of the plaque to rupture and cause catastrophic events. The need to distinguish normal fat and cholesterol may not be critical as both typically are contained in the lipid-rich necrotic core and exhibit similar electrical properties [18]. Therefore, by focusing on lipid detection, the OEIT device positions itself in identifying the key composition indicator for the risk of plaque rupturing, and fat tissue is a reasonable approximation for testing OEIT functionality in our *ex vivo* phantom set-up.

The drastically different level of conductivity of lipid compared to normal tissue is essential for the application potential of OEIT. As a comparison, the most commonly adopted imaging procedure is angiogram followed by FFR, which could only assess the plaque vulnerability through degree of obstruction (i.e. estimating the size of the plaques). Such criterion has been found less correlating to the actual risk of plaque rupturing [2, 9], whereas impedimetric signature has been shown to indicate distinct lesion severity using EIS-based sensing [19]. OEIT, by offering a full intravascular cross-sectional image, is aimed to present significant advancement from those existing impedance spectrum-based techniques that mostly only provide localized measurement within the vessel wall or extremely coarse coverage of the whole vessel [16, 17]. Furthermore, with recent evidence indicating an important role by perivascular fatty tissue in revealing early vascular inflammation and plaque vulnerability [39], we also believe OEIT is in principle capable of observing beyond the vessel wall and targeting perivascular fat by extending the DOI as shown in section III-D (Fig. 7c). Another potentially important aspect for atherosclerosis characterization is the calcification within atherosclerotic lesions. The role calcification plays in determining the vulnerability of these lesions is less apparent compared to the thinning of fibrous cap and growing of necrotic core, and still under debate [3, 40]. Yet given the prevalence of calcification in atherosclerotic plaques, it would be desirable for an intravascular imaging modality to be capable of identifying calcification. We are hopeful that OEIT can be used to examine calcified lesion as well. First, we anticipate the calcified region to exhibit high impedance values due to their similar formation process and material composition as bone [41], a less conductive material [18]. This makes calcified region easy to separate from cell-rich region (low impedance) within the lesion under impedance tomography. There will be challenges as to differentiate calcified and lipid-rich regions. One strategy is to vary the

interrogating frequency to probe the different response and subsequently apply differential EIT algorithm [42] to separate these two types of materials.

Our group has been pursuing catheter-based intravascular devices integrating electrical or other sensing capabilities [43]. Our previous percutaneous intervention study on animals demonstrated the compatibility of such devices with routine catheterization operation [17]. These efforts lay the foundation for live animal testing towards translational application of OEIT in the near future. One important aspect along this vein is to downsize the current version of OEIT device. In our previous work, we managed to fabricate a catheter device equipped with impedance sensing electrodes with ~1.3 mm overall diameter and has been successfully inserted into the rabbit aorta through a 4-French sheath [17]. The key component to accommodate the electrode deployment on the catheter is the inflatable miniaturized balloon. With the current state of art fabrication techniques, highly flexible electrodes can be made and affixed on the surface of the balloon. By deflating the balloon, the cross-sectional dimension of the catheter can be kept at small value, while the balloon can be inflated after the catheter has advanced to the target location. It has also been demonstrated by others that large number of individual electrodes can be placed on the balloon (>32) [35], such that the impedance data is sufficient to enable electrical impedance tomography with high resolution. The pitch between individual electrodes can be <0.1 mm through standard microfabrication process, which translate to an overall diameter of ~1 mm with 32 electrodes. On the other hand the inflatable feature of the balloon is also particularly helpful for electrical sensing as electrodes being in contact with the vessel wall is a more desired scenario than surrounded by conductive blood flow, which could mask out electrical signal measurement significantly. Our OEIT device is also amendable to such configuration, although certain concerns require further consideration. For instance, touching the vessel wall and potentially the plaques itself could induce higher risk of plaque rupturing due to any mechanical disturbance during the measuring procedure. A balance needs to be achieved between the signal quality and the proximity between electrodes and plaques. Overall, we hope to demonstrate the promising capability of OEIT with all the above experiments and we are in great position to further pursue *in vivo* study.

It is also important to note that there is still plenty of room for improving the imaging resolution and tissue specificity of OEIT. Firstly, during the lipid identification experiment and subsequent imaging, a concentric configuration between the device and the aorta was assumed. The distance between the sensing electrodes and the lesion could influence the measurement and overall imaging performance. A strategy with careful calibration experiment and signal normalization algorithm used in a recent intracoronary near infrared autofluorescence study [44] can also be adapted in our setting to improve device functionality. Moreover, the recently popular multimodal approach [10] is worth further exploration. We have previously demonstrated the idea of linking MRI information as *a priori* input for further refinement of conductivity mapping, albeit in a non-invasive setting aimed at fatty liver characterization [30]. The combination of OEIT with other imaging modalities (e.g. IVUS or OCT) could potentially achieve comprehensive *in vivo* characterization of plaques with high precision and deep coverage through the synergetic functioning from different modalities. The low-cost and relative ease of hardware implementation of OEIT make it rather amenable for such integration.

The major challenges for such multi-modal device integration includes both hardware and software aspects: for hardware, there is an overall dimension limit for this type of invasive catheter devices to be deployed for intravascular diagnosis. It will be challenging to downsize the current version of OEIT with 32 individual electrodes and also accommodate all the wiring and components required by another modalities. We have experience previously in assembling simple impedance sensing with IVUS probe [43]. To bring such multiple-modal catheter device to meet translational standard would require careful planning for overall device design, wire routing, and component configuration, instead of mechanistically putting separate sensor together. On the software front, there are also questions needed to be answered with continuing effort along the path. For instance, the overall strategy in using such multi-modal catheter needs to be decided. We can simply let different modalities perform their own functions and co-register the imaging result to capture all the features that can only be obtained by each individual method. We can also use the information obtained from one modality as *a prior* input to improve the imaging results of the other. For the former strategy, further questions include whether we simply let the cardiologist to interpret all the available results made for them and make final judgement, or we can rely even more on algorithm (e.g. machine learning techniques) to extract useful information directly. For the latter, mathematical details need to be worked out to optimize such process, and since intravascular imaging would ideally require real time operation, the time consumption issue will demand more attention.

Furthermore, the implementation of OEIT with "outward facing" electrodes to target tubular objects presented a paradigm shift from the dominant usage of EIT for human thoracic imaging, with tremendous implication beyond the potential in intravascular imaging. The prototypical devices proposed by Halter et al. for prostate tumor detection and laparoscopic prostatectomy demonstrated another possibility [26, 27]. Another great application is the endoscopic interrogation in the gastrointestinal tract, with detecting tumor being a primary target as tumorous tissue also exhibits distinct electrical signature from normal tissue. With the advancement of microfabrication and flexible electronics, the technology integrating a large number of electrodes with varying dimensions on a catheter device is available to meet the requirement depending on the actual size of the tissue under investigation and the resolution required for diagnosis.

V. Conclusion

In this work, we presented a novel intravascular imaging modality, OEIT. We first studied the feasibility of image reconstruction in such a non-conventional configuration through a simulation model. We then investigated the characteristics of the OEIT device in predefined boundary experimental settings. We further advanced to use an *ex vivo* phantom built to emulate practical conditions to demonstrate the proximity detection function and plaque identification. The success in *ex vivo* imaging paves the way for the further adaptation of OEIT for live animal *in vivo* studies and potentially human trials. We envision this novel imaging modality can evolve to become a powerful alternative for intravascular diagnosis and seek broader applications in endoscopic operations.

Supplementary Material

Refer to Web version on PubMed Central for supplementary material.

Acknowledgment

Reference

[1]. Tomey MI, Narula J, and Kovacic JC, "Advances in the understanding of plaque composition and treatment options: year in review," J. Am. Coll. Cardiol, vol. 63, no. 16, pp. 1604–1616, 2014. [PubMed: 24583311]

[2]. Bentzon JF, Otsuka F, Virmani R, and Falk E, "Mechanisms of plaque formation and rupture," Circ. Res, vol. 114, no. 12, pp. 1852–1866, 2014. [PubMed: 24902970]

[3]. Yahagi K et al. , "Pathophysiology of native coronary, vein graft, and in-stent atherosclerosis," Nat. Rev. Cardiol, vol. 13, no. 2, p. 79, 2016. [PubMed: 26503410]

[4]. WHO, "The top 10 causes of death. 2014," Fact sheet, no. 310, 2018.

[5]. Goel S et al. , "Imaging modalities to identity inflammation in an atherosclerotic plaque," Radiol. Res. Pract, vol. 2015, 2015.

[6]. Dweck MR et al. , "Imaging of coronary atherosclerosis—evolution towards new treatment strategies," Nat. Rev. Cardiol, vol. 13, no. 9, p. 533, 2016. [PubMed: 27226154]

[7]. Tarkin JM et al. , "Imaging atherosclerosis," Circ. Res, vol. 118, no. 4, pp. 750–769, 2016. [PubMed: 26892971]

[8]. Mehanna E, Li J, Patel S, and Parikh SA, "The Future of Intravascular Imaging: Are We Primed to Detect Vulnerable Plaques?," Curr. Cardiovasc. Imaging Rep, vol. 10, no. 4, p. 10, 2017.

[9]. Syed MB et al. , "Emerging techniques in atherosclerosis imaging," Brit. J. Radiol, vol. 92, no. 1103, p. 20180309, 2019. [PubMed: 31502858]

[10]. Ma T, Zhou B, Hsiai TK, and Shung KK, "A review of intravascular ultrasound-based multimodal intravascular imaging: the synergistic approach to characterizing vulnerable plaques," Ultrason. Imaging, vol. 38, no. 5, pp. 314–331, 2016. [PubMed: 26400676]

[11]. Jorge E et al. , "Optical coherence tomography of the pulmonary arteries: A systematic review," J. Cardiol, vol. 67, no. 1, pp. 6–14, 2016. [PubMed: 26572955]

[12]. Layland J, Wilson A, Lim I, and Whitbourn R, "Virtual histology: a window to the heart of atherosclerosis," Heart Lung Circ, vol. 20, no. 10, pp. 615–621, 2011. [PubMed: 21276753]

[13]. Swamy PM, Mamas MA, and Bharadwaj AS, "Role of Near-Infrared Spectroscopy (NIRS) in Intracoronary Imaging," Curr. Cardiovasc. Imaging Rep, vol. 12, no. 8, p. 34, 2019.

[14]. Streitner I et al. , "Electric impedance spectroscopy of human atherosclerotic lesions," Atherosclerosis, vol. 206, no. 2, pp. 464–468, 2009. [PubMed: 19419719]

[15]. Streitner I et al. , "Cellular imaging of human atherosclerotic lesions by intravascular electric impedance spectroscopy," PLoS One, vol. 7, no. 4, 2012.

[16]. Packard RRS et al. , "Two-point stretchable electrode array for endoluminal electrochemical impedance spectroscopy measurements of lipid-laden atherosclerotic plaques," Ann. Biomed. Eng, vol. 44, no. 9, pp. 2695–2706, 2016. [PubMed: 26857007]

[17]. Packard RRS et al. , "3-D electrochemical impedance spectroscopy mapping of arteries to detect metabolically active but angiographically invisible atherosclerotic lesions," Theranostics, vol. 7, no. 9, p. 2431, 2017. [PubMed: 28744325]

[18]. Hasgall P et al. , "IT'IS Database for thermal and electromagnetic parameters of biological tissues," Version 4.0, May 15, 2018, DOI: 10.13099/VIP21000-04-0.itis.swiss/database.

[19]. Yu F, Dai X, Beebe T, and Hsiai T, "Electrochemical impedance spectroscopy to characterize inflammatory atherosclerotic plaques," Biosens. Bioelectron, vol. 30, no. 1, pp. 165–173, 2011. [PubMed: 21959227]

[20]. Holder D, Electrical impedance tomography: methods, history and applications. CRC Press, 2004.

[21]. Adler A and Boyle A, "Electrical impedance tomography: Tissue properties to image measures," IEEE Trans. Biomed. Eng, vol. 64, no. 11, pp. 2494–2504, 2017. [PubMed: 28715324]

[22]. Adler A et al. , "Whither lung EIT: where are we, where do we want to go and what do we need to get there?," Physiol. Meas, vol. 33, no. 5, p. 679, 2012. [PubMed: 22532268]

[23]. Aristovich KY, dos Santos GS, Packham BC, and Holder DS, "A method for reconstructing tomographic images of evoked neural activity with electrical impedance tomography using intracranial planar arrays," Physiol. Meas, vol. 35, no. 6, p. 1095, 2014. [PubMed: 24845144]

[24]. Boverman G, Kao T-J, Wang X, Ashe JM, Davenport DM, and Amm BC, "Detection of small bleeds in the brain with electrical impedance tomography," Physiol. Meas, vol. 37, no. 6, p. 727, 2016. [PubMed: 27203851]

[25]. Murphy EK, Mahara A, and Halter RJ, "A novel regularization technique for microendoscopic electrical impedance tomography," IEEE Trans. Med. Imaging, vol. 35, no. 7, pp. 1593–1603, 2016. [PubMed: 26812707]

[26]. Wan Y et al. , "Transrectal electrical impedance tomography of the prostate: spatially coregistered pathological findings for prostate cancer detection," Med. Phys, vol. 40, no. 6Part1, p. 063102, 2013. [PubMed: 23718610]

[27]. Mahara A, Khan S, Murphy EK, Schned AR, Hyams ES, and Halter RJ, "3D microendoscopic electrical impedance tomography for margin assessment during robot-assisted laparoscopic prostatectomy," IEEE Trans. Med. Imaging, vol. 34, no. 7, pp. 1590–1601, 2015. [PubMed: 25730825]

[28]. Yang F and Patterson RP, "A novel impedance-based tomography approach for stenotic plaque detection: A simulation study," Int. J. Cardiol, vol. 144, no. 2, pp. 279–283, 2010. [PubMed: 19251327]

[29]. Chakraborty D and Chattopadhyay M, "Finite element method based modeling of a sensory system for detection of atherosclerosis in human using electrical impedance tomography," Procedia Technology, vol. 10, pp. 262–270, 2013.

[30]. Luo Y et al. , "Non-invasive electrical impedance tomography for multi-scale detection of liver fat content," Theranostics, vol. 8, no. 6, p. 1636, 2018. [PubMed: 29556346]

[31]. Adler A et al. , "EIDORS Version 3.8," in Proc. of the 16th Int. Conf. on Biomedical Applications of Electrical Impedance Tomography, 2015.

[32]. Guo R, Ren Z, Bi H, Xu M, and Cai L, "Electrical and thermal conductivity of polylactic acid (PLA)-based biocomposites by incorporation of nano-graphite fabricated with fused deposition modeling," Polymers, vol. 11, no. 3, p. 549, 2019.

[33]. Chen B et al. , "Characterization of atherosclerotic plaque in patients with unstable angina pectoris and stable angina pectoris by optical coherence tomography," Zhonghua xin xue guan bing za zhi, vol. 37, no. 5, pp. 422–425, 2009. [PubMed: 19781218]

[34]. Huang Z-Y, Luo Y, Abiri P, Packard RR, Hsiai TK, and Tai Y-C, "Double-Ballooned Local Drug Delivery Catheter with Blood Bypassing Function," in 2019 20th International Conference on Solid-State Sensors, Actuators and Microsystems & Eurosensors XXXIII (TRANSDUCERS & EUROSENSORS XXXIII), 2019: IEEE, pp. 2213–2216.

[35]. Kim D-H et al. , "Materials for multifunctional balloon catheters with capabilities in cardiac electrophysiological mapping and ablation therapy," Nature materials, vol. 10, no. 4, pp. 316–323, 2011. [PubMed: 21378969]

[36]. Ota H et al. , "Quantitative vascular measurements in arterial occlusive disease," Radiographics, vol. 25, no. 5, pp. 1141–1158, 2005. [PubMed: 16160101]

[37]. Leipsic J et al. , "SCCT guidelines for the interpretation and reporting of coronary CT angiography: a report of the Society of Cardiovascular Computed Tomography Guidelines Committee," Journal of cardiovascular computed tomography, vol. 8, no. 5, pp. 342–358, 2014. [PubMed: 25301040]

[38]. Jasti V, Ivan E, Yalamanchili V, Wongpraparut N, and Leesar MA, "Correlations between fractional flow reserve and intravascular ultrasound in patients with an ambiguous left main coronary artery stenosis," Circulation, vol. 110, no. 18, pp. 2831–2836, 2004. [PubMed: 15492302]

[39]. Antonopoulos AS et al. , "Detecting human coronary inflammation by imaging perivascular fat," Sci. Transl. Med, vol. 9, no. 398, 2017.

[40]. Alexopoulos N and Raggi P, "Calcification in atherosclerosis," Nature Reviews Cardiology, vol. 6, no. 11, pp. 681–688, 2009. [PubMed: 19786983]

[41]. Johnson RC, Leopold JA, and Loscalzo J, "Vascular calcification: pathobiological mechanisms and clinical implications," Circulation research, vol. 99, no. 10, pp. 1044–1059, 2006. [PubMed: 17095733]

[42]. Seo JK and Woo EJ, Nonlinear inverse problems in imaging. John Wiley & Sons, 2012.

[43]. Ma J et al. , "Ultrasonic transducer-guided electrochemical impedance spectroscopy to assess lipid-laden plaques," Sensors and Actuators B: Chemical, vol. 235, pp. 154–161, 2016.

[44]. Athanasiou L et al., "Intracoronary near infrared autofluorescence signal calibration," in 2020 42nd Annual International Conference of the IEEE Engineering in Medicine & Biology Society (EMBC), 2020, pp. 1871–1874: IEEE.
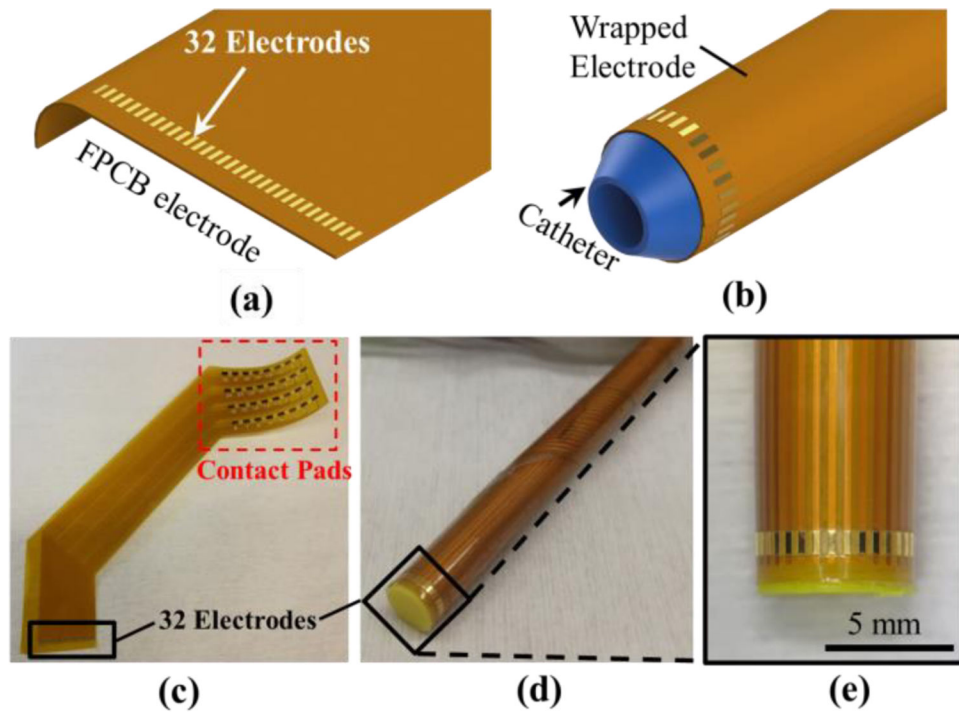
Fig. 1.
The Outward Electrical Impedance Tomography (OEIT) device: (a)&(b) the schematic illustration of the 32-electrodes flexible PCB and device assembly by wrapping it around a cylindrical catheter. (c) Image of the flexible PCB before wrapping, (d) final assembly of the OEIT device with close-up view on the individual electrodes (e).
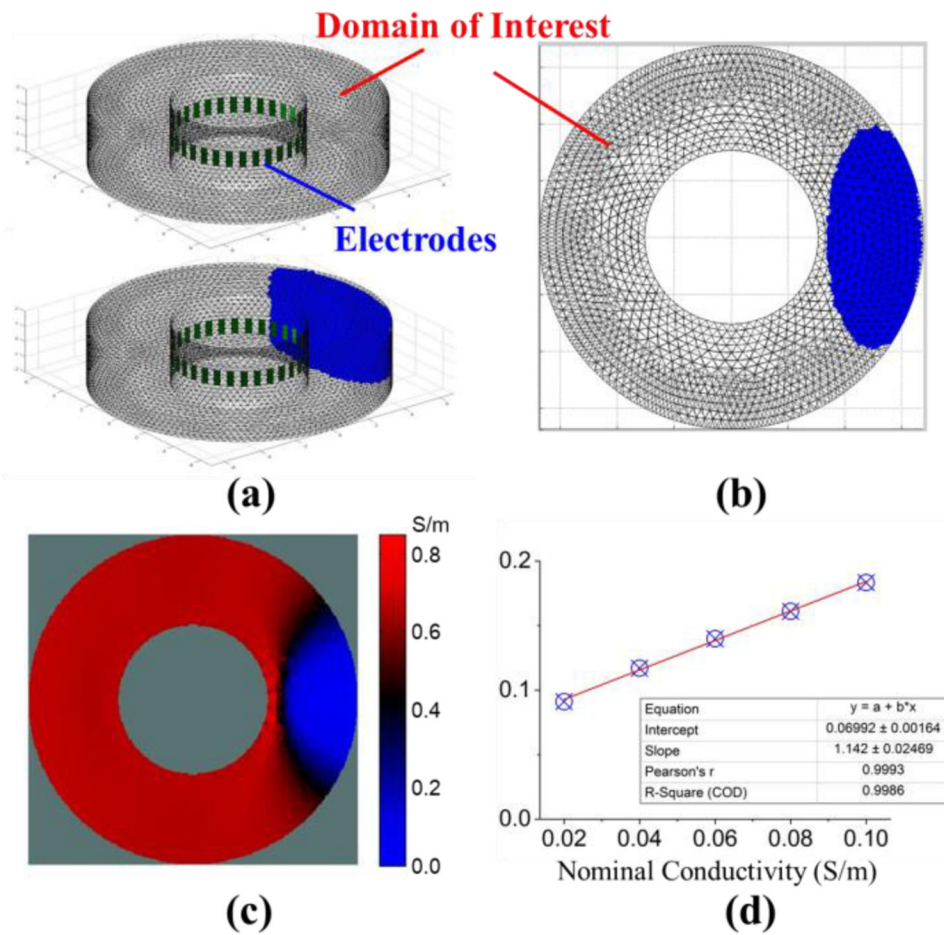
Fig. 2.
Simulation study: (a) the 3D model and meshing created in EIDORS with and without the ellipsoid region to mimic fatty tissue, (b) top view of the model, (c) representative imaging result obtained from the model and (d) the comparison between nominal and calculated conductivity from the model simulation, linear fitting with r>0.99
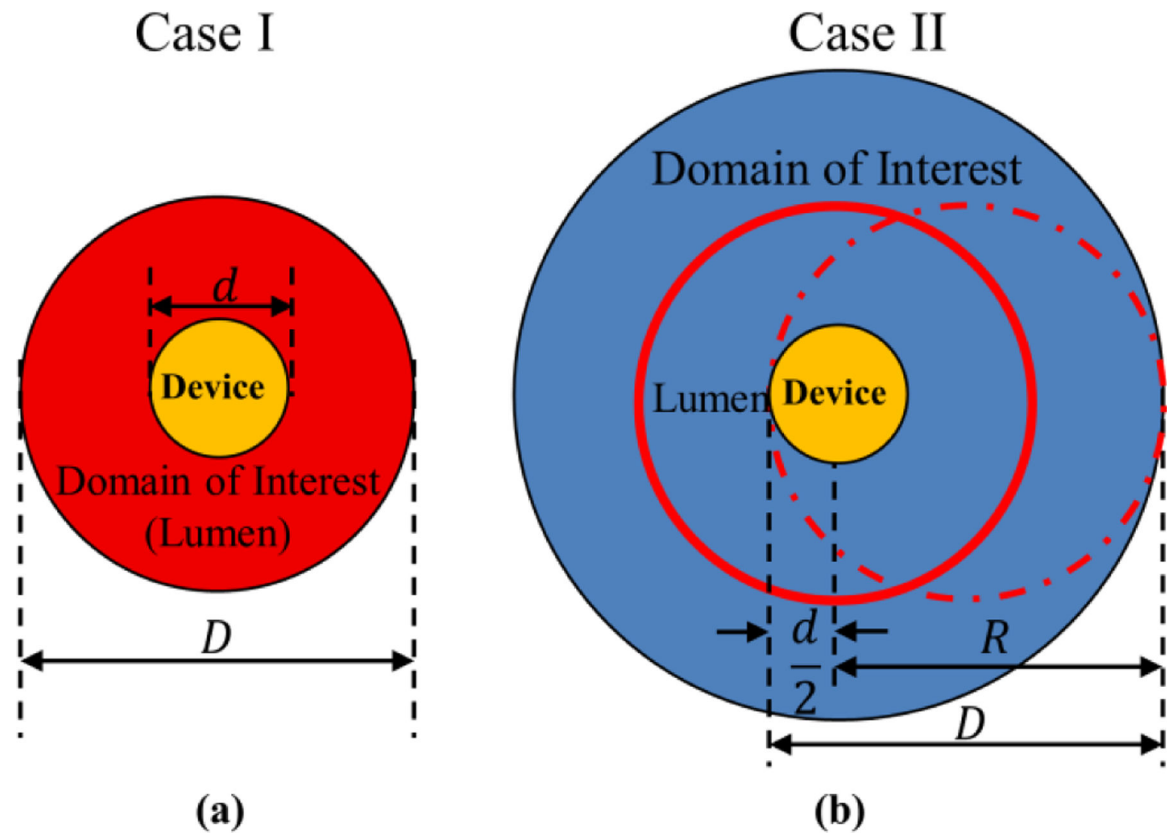
Fig. 3.

Two scenarios for model construction: (a) Case I: The domain of interest has diameter D equal to the vessel diameter (~13.5 mm); (b) Case II: the domain of interest should has radius $R \geq D - \frac{d}{2}$ (see the dotted circle for the extreme condition), in the actual model we directly use $R = D$
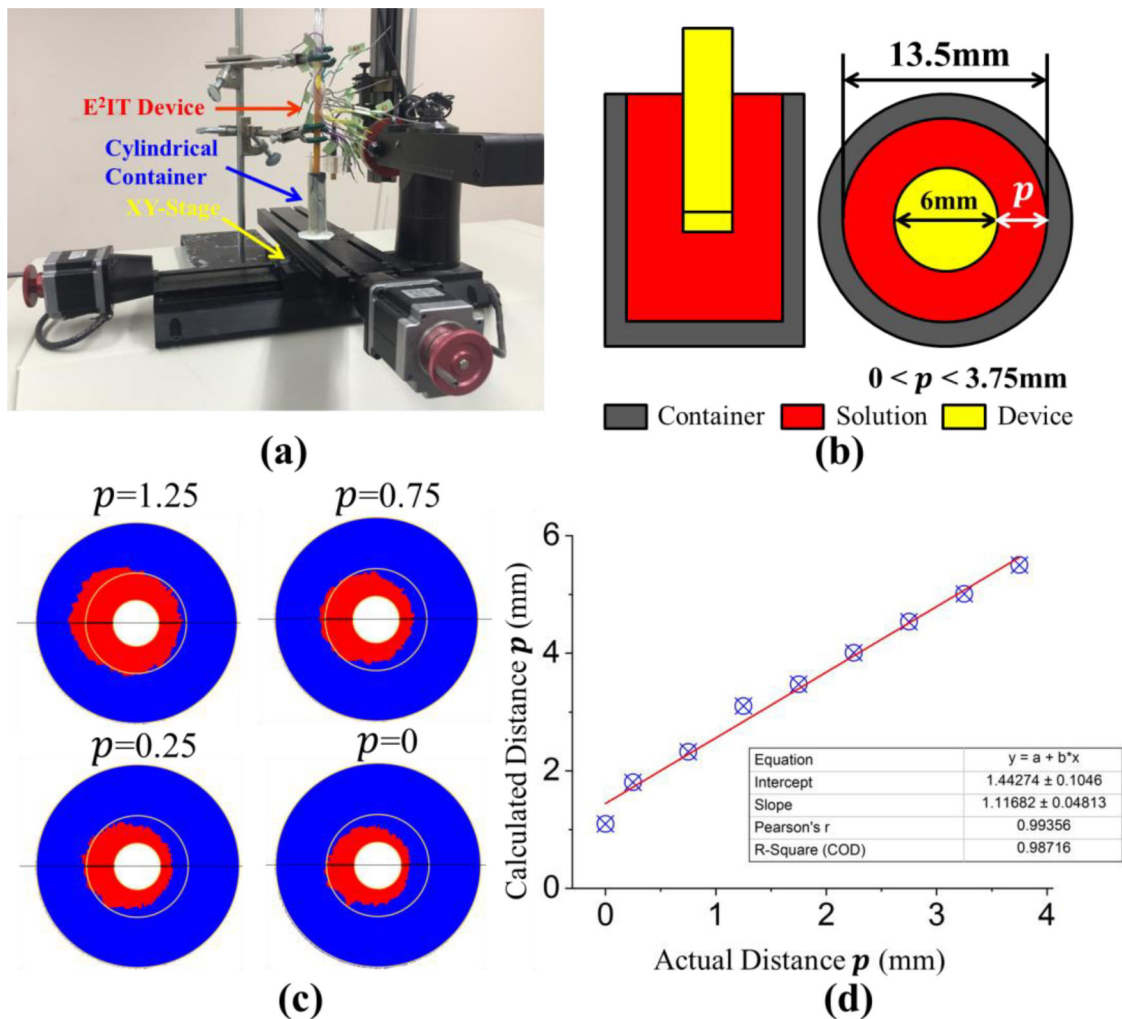
Fig. 4.
Proximity measurement: (a) Overall experimental set-up showing the OEIT Device, the container and the XY-stage with their configuration illustrated in (b) highlighting key parameters. (c) selected imaging results from the proximity measurement and (d) a comparison between the actual distance *p* and the value obtained from imaging results. Linear fitting with r>0.99.
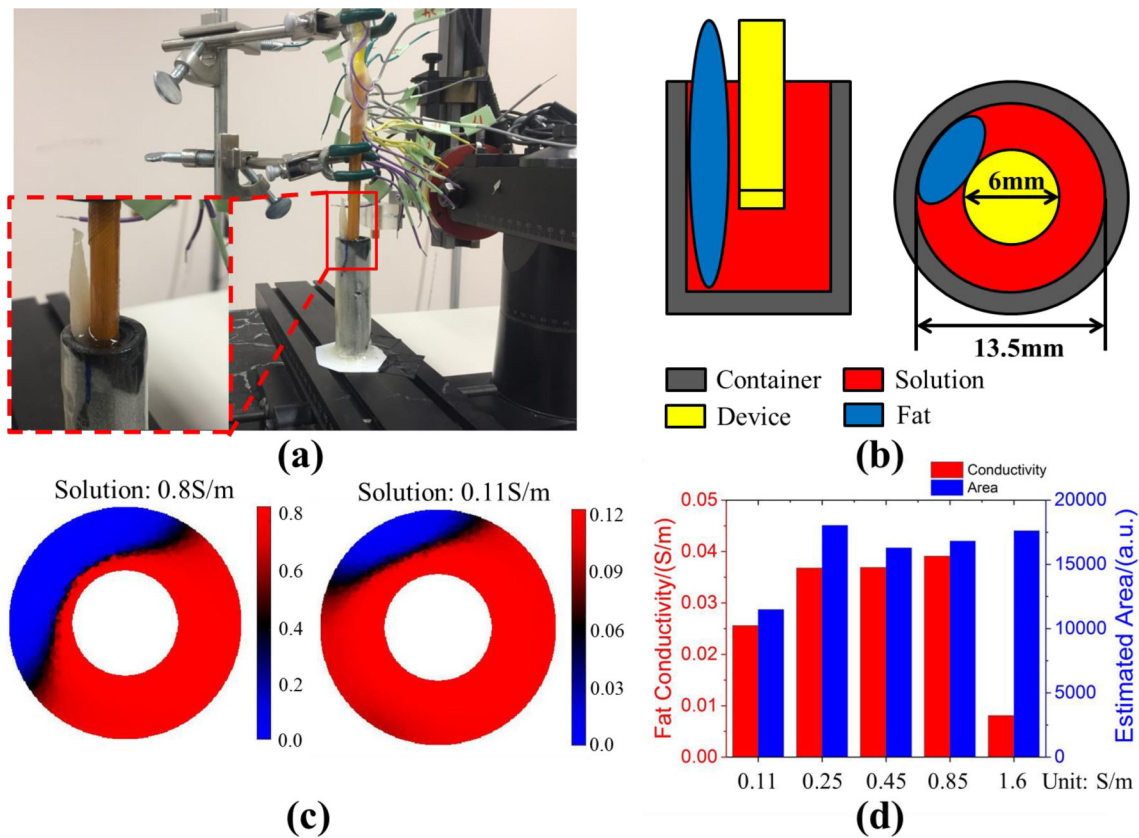
Fig. 5.

Conductivity Characterization: (a) Image showing experimental set-up for the testing with close-up view on the fatty tissue immersed in the solution and (b) schematic illustration of object configuration and key parameters. (c) Two selected imaging results from the experiment and (d) plot of average conductivity and occupied area calculated from the imaging for all conductivity conditions.
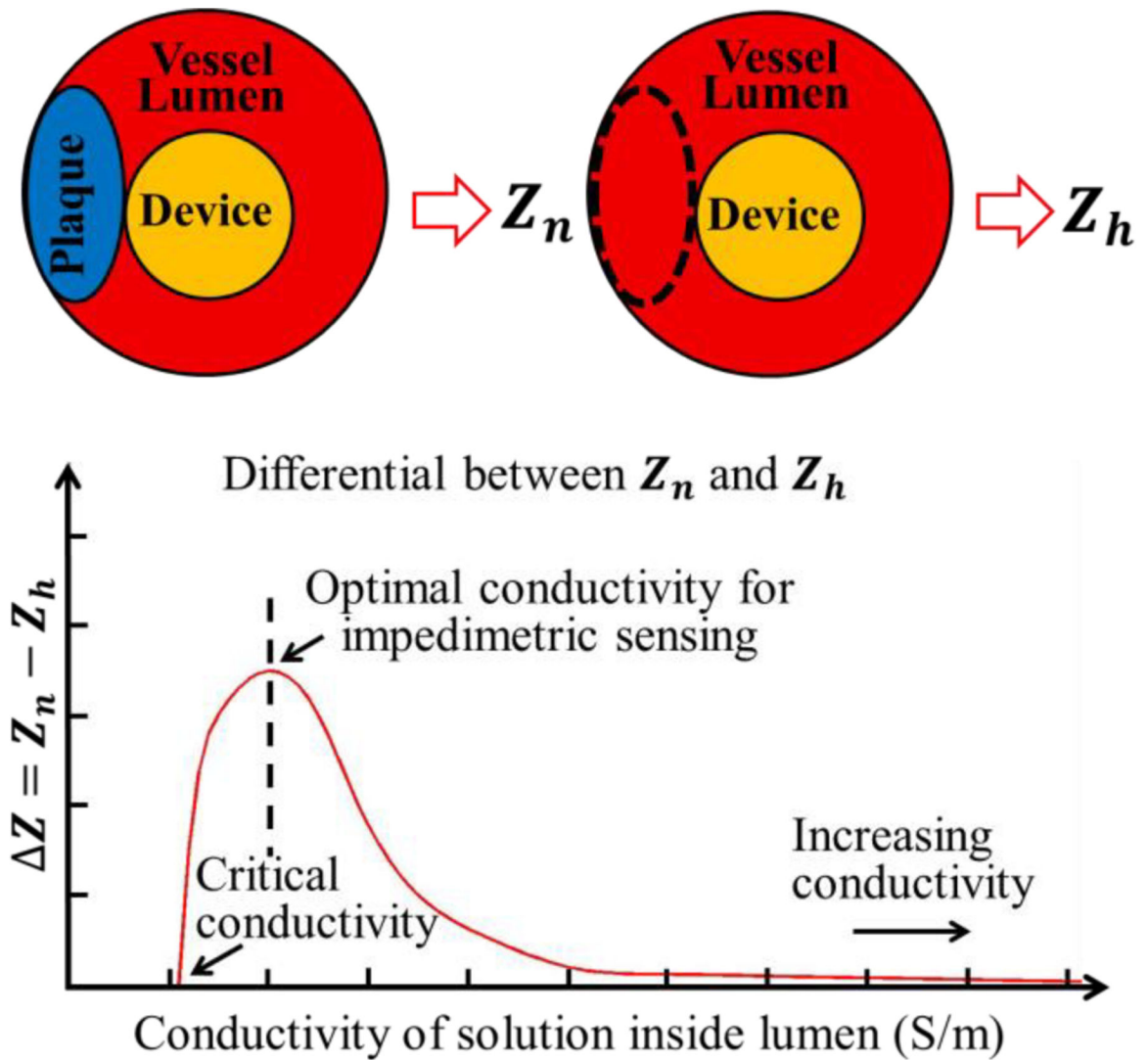
Fig. 6.
Schematic illustration and a conceptual curve demonstrating the hypothesis in section III-C, Z_p, Z_b, and Z only represent a conceptual impedimetric sensing data, not specifically pertaining to EIS or EIT.
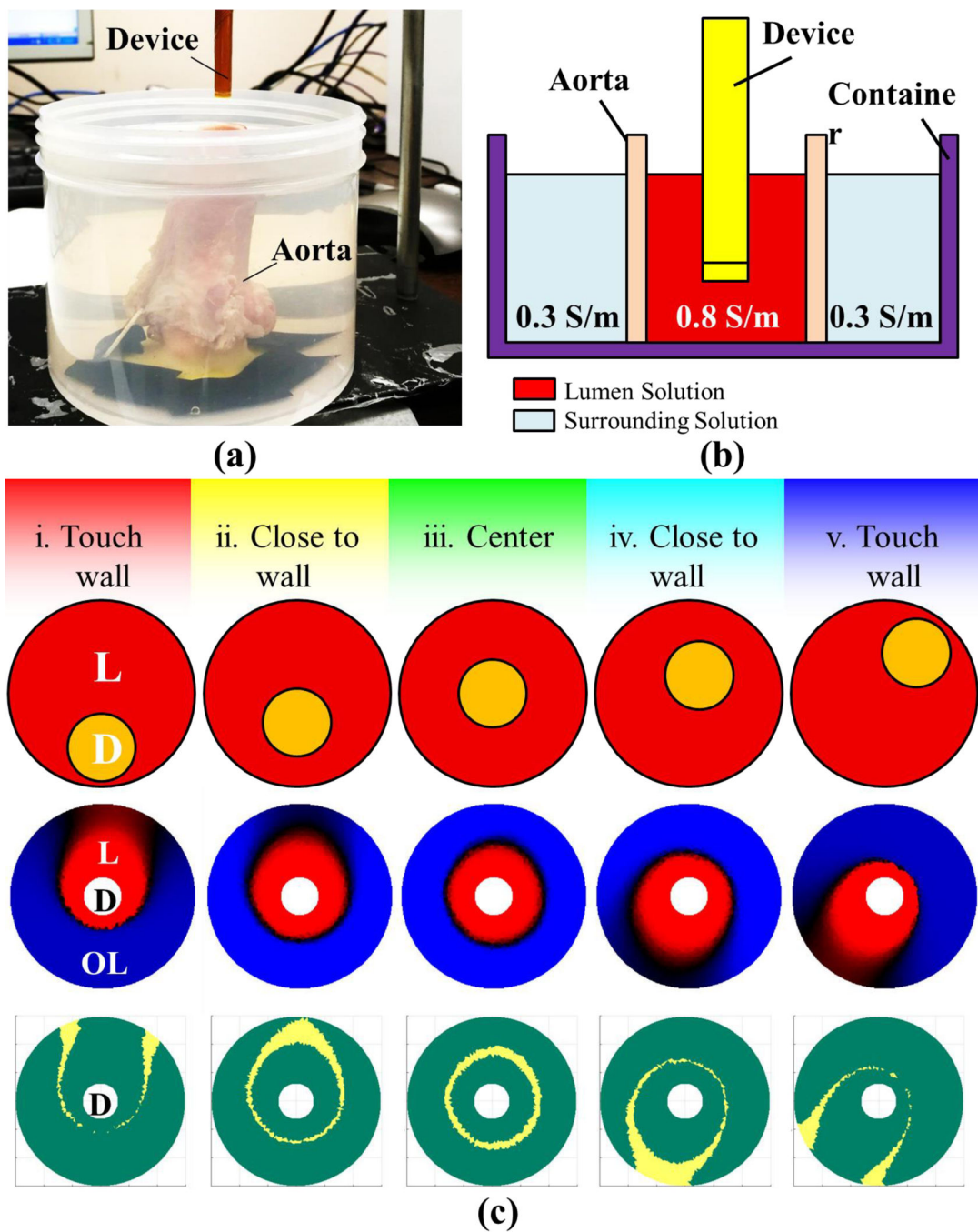
Fig. 7.
Proximity detection in aorta: (a) Image showing experimental set-up for the testing and (b) schematic illustration of object configuration and key parameters. (c) A sequence of imaging results identifying different relative positions between the device and aorta, upper panels: schematics, middle panels: initial imaging results, lower panels: traces representing aorta wall. L = Lumen, D = Device, OL = Outside Lumen
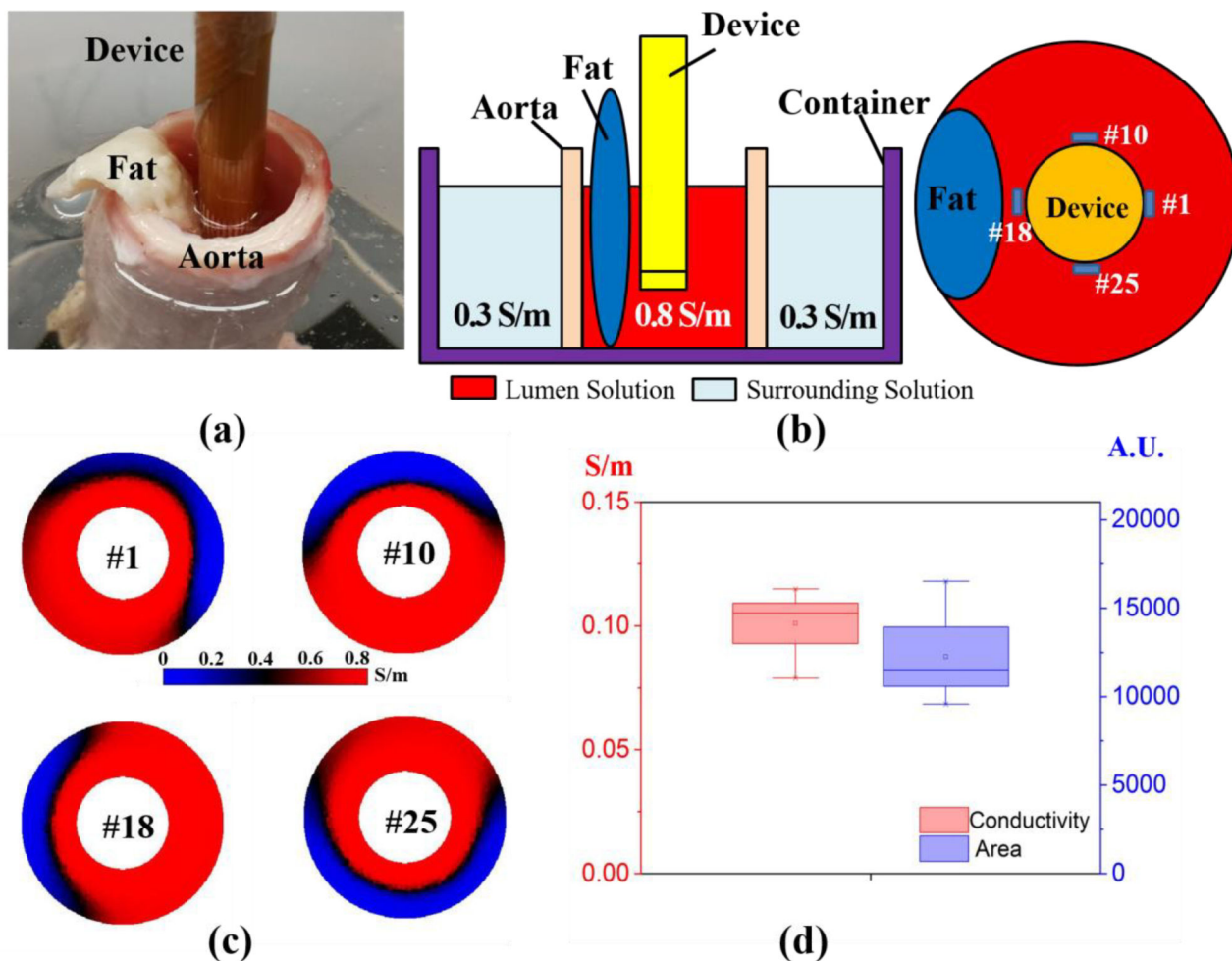
Fig. 8.
Lipid identification in aorta: (a) Image of close-up view for the fat tissue placement inside the aorta and (b) the detail configuration schematic. (c) Imaging results from four different fat placement showing the clear identification and (d) Average conductivity and estimated area from the region of interest generated using the imaging results
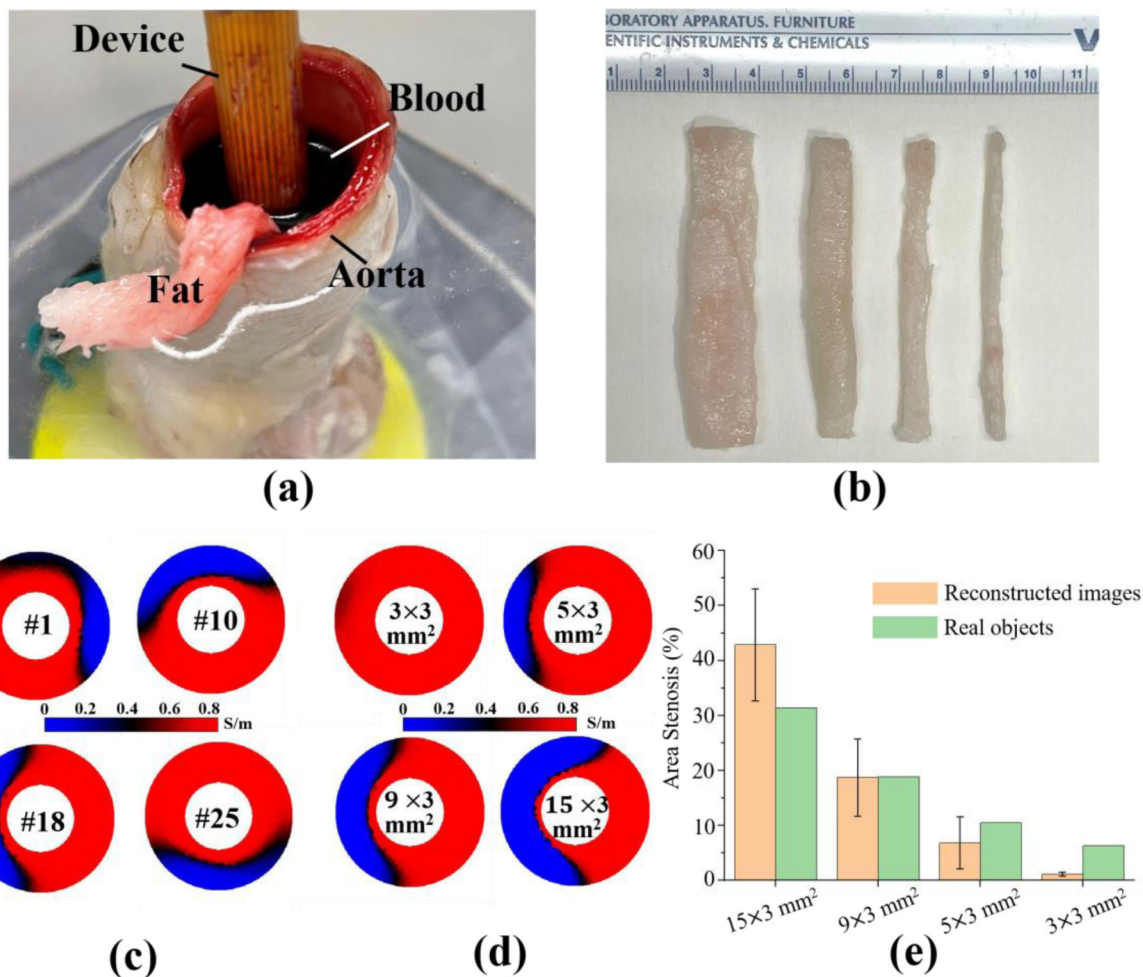
Fig. 9.

Lipid identification in real blood with different sizes: (a) Image of close-up view for the fat tissue placement inside the aorta filled with real blood and (b) fat tissue with four different sizes. (c) Imaging results from four different fat placement, and (d) imaging results from four different sizes placed on the same location. (e) Comparison of area stenosis between real sample and tomographic imaging extracted results.